



Automated computerized image analysis for the user-independent evaluation of disease severity in preclinical models of NAFLD/NASH

Maxime De Rudder¹ · Caroline Bouzin ² · Maxime Nachit^{1,3} · Heloïse Louveigny¹ · Greetje Vande Velde ³ · Yvon Julé⁴ · Isabelle A. Leclercq ¹

Received: 7 May 2019 / Revised: 25 July 2019 / Accepted: 14 August 2019
© United States & Canadian Academy of Pathology 2019

Abstract

Pathologists use a semiquantitative scoring system (NAS or SAF score) to facilitate the reporting of disease severity and evolution. Similar scores are applied for the same purposes in rodents. Histological scores have inherent inter- and intra-observer variability and yield discrete and not continuous values. Here we performed an automatic numerical quantification of NASH features on liver sections in common preclinical NAFLD/NASH models. High-fat diet-fed *foz/foz* mice (Foz HF) or wild-type mice (WT HF) known to develop progressive NASH or an uncomplicated steatosis, respectively, and C57Bl6 mice fed a choline-deficient high-fat diet (CDAA) to induce steatohepatitis were analyzed at various time points. Automated software image analysis of steatosis, inflammation, and fibrosis was performed on digital images from entire liver sections. Data obtained were compared with the NAS score, biochemical quantification, and gene expression. As histologically assessed, WT HF mice had normal liver up to week 34 when they harbor mild steatosis with if any, little inflammation. Foz HF mice exhibited grade 2 steatosis as early as week 4, grade 3 steatosis at week 12 up to week 34; inflammation and ballooning increased gradually with time. Automated measurement of steatosis (macrovesicular steatosis area) revealed a strong correlation with steatosis scores ($r = 0.89$), micro-CT liver density, liver lipid content ($r = 0.89$), and gene expression of CD36 ($r = 0.87$). Automatic assessment of the number of F4/80-immunolabelled crown-like structures strongly correlated with conventional inflammatory scores ($r = 0.79$). In Foz HF mice, collagen deposition, evident at week 20 and progressing at week 34, was automatically quantified on picrosirius red-stained entire liver sections. The automated procedure also faithfully captured and quantitated macrovesicular steatosis, mixed inflammation, and pericellular fibrosis in CDAA-induced steatohepatitis. In conclusion, the automatic numerical analysis represents a promising quantitative method to rapidly monitor NAFLD activity with high-throughput in large preclinical studies and for accurate monitoring of disease evolution.

Supplementary information The online version of this article (<https://doi.org/10.1038/s41374-019-0315-9>) contains supplementary material, which is available to authorized users.

✉ Isabelle A. Leclercq
isabelle.leclercq@uclouvain.be

- ¹ Laboratory of Hepato-Gastroenterology, Institut de Recherche Expérimentale et Clinique, Université catholique de Louvain (UCLouvain), Brussels, Belgium
- ² Imaging platform 2IP, Institut de Recherche Expérimentale et Clinique, Université catholique de Louvain (UCLouvain), Brussels, Belgium
- ³ Department of Imaging and Pathology, Faculty of Medicine & MoSAIC, Biomedical Sciences, KU Leuven, Leuven, Belgium
- ⁴ Biocellvia, Marseille, France

Introduction

Nonalcoholic fatty liver disease (NAFLD) is the hepatic complication of obesity and metabolic syndrome and now the most common chronic liver disease in the world [1]. As many as 116 million people in the EU alone may suffer from NAFLD (25% of the general population, 90% of obese subjects) (EASL statement 2017). NAFLD represents a spectrum of diseases ranging from benign steatosis to nonalcoholic steatohepatitis (NASH), in which hepatocellular injury and inflammation promote fibrosis and evolution to end-stage liver disease. It is estimated that between 20 and 50% of NAFLD patients have NASH [1].

The gold standard for NASH diagnosis is the liver biopsy. The diagnosis is based on pattern recognition by the pathologist followed by the evaluation of the severity of

individual histological criteria, namely liver steatosis, lobular or portal inflammation, hepatocellular injury including cell death and predeath (coined by hepatocyte ballooning), and staging of fibrosis. Scores, such as NAS or SAF, are compilations of such criteria and were developed as tools to measure changes in NAFLD during therapeutic trials [2, 3]. A reduction in at least 2 points in NAS can be an acceptable marker of disease improvement if it is associated with no progression in fibrosis [4, 5]. However, it is still ill-defined whether resolution of NASH with no worsening of fibrosis (assessed as an increase in the fibrosis stage), improvement of lobular inflammation and cell death, or improvement in fibrosis with no progression of steatohepatitis (i.e., no increase in activity as assessed by NAS) better predict the outcome [5].

The histology-based NAS scoring system is dependent on the subjective evaluation by the pathologist and therefore subject to intra- and inter-reader variability [2, 6–8]. Also, the range of grading scores is limited. Importantly, data support that disease evolution, and singularly fibrosis evolution, is not linear [9] and therefore change in fibrosis may not be satisfactorily captured by a scoring system even if the impact on the disease and overall health could be important. Hence, histological semiquantitative scores may not accurately capture the evolution of NAFLD/NASH severity and consequently precisely quantify the effectiveness of pharmacological treatments.

Objective and continuous measurement would overcome these limitations. Computerized image analyses are used for this purpose in noninvasive imaging techniques, such as Magnetic resonance imaging (MRI), computed tomography (CT-scan), and ultrasounds [10, 11] applied widely for clinical investigations. MRI-derived sequences, such as MRI PDFF (Proton density fat fraction) and Magnetic resonance elastography, are the current noninvasive gold standard for assessing steatosis and fibrosis, respectively [10, 12, 13]. Transient elastography combined with controlled attenuation parameter is the point-of-care technique to diagnose advanced fibrosis and cirrhosis and accurately grade steatosis (AUROC of 0.91, 0.95, and 0.89 for steatosis grades 1, 2, and 3, respectively) at the patient's bed. The technique is however suboptimal for low steatosis or fibrosis scores [10, 12, 13]. Importantly, in spite of promising developments [14, 15], none of the noninvasive imaging modalities reliably discriminates NASH from simple steatosis, largely due to the limited power for detecting inflammation and hepatocellular injury. Therefore, to date, histopathological evaluation remains a key for diagnosis.

Computerized image techniques were also developed for the morphometrical assessment of NAFLD/NASH histology, particularly steatosis [16–20], and fibrosis [21]; the advantage being to provide an operator-independent

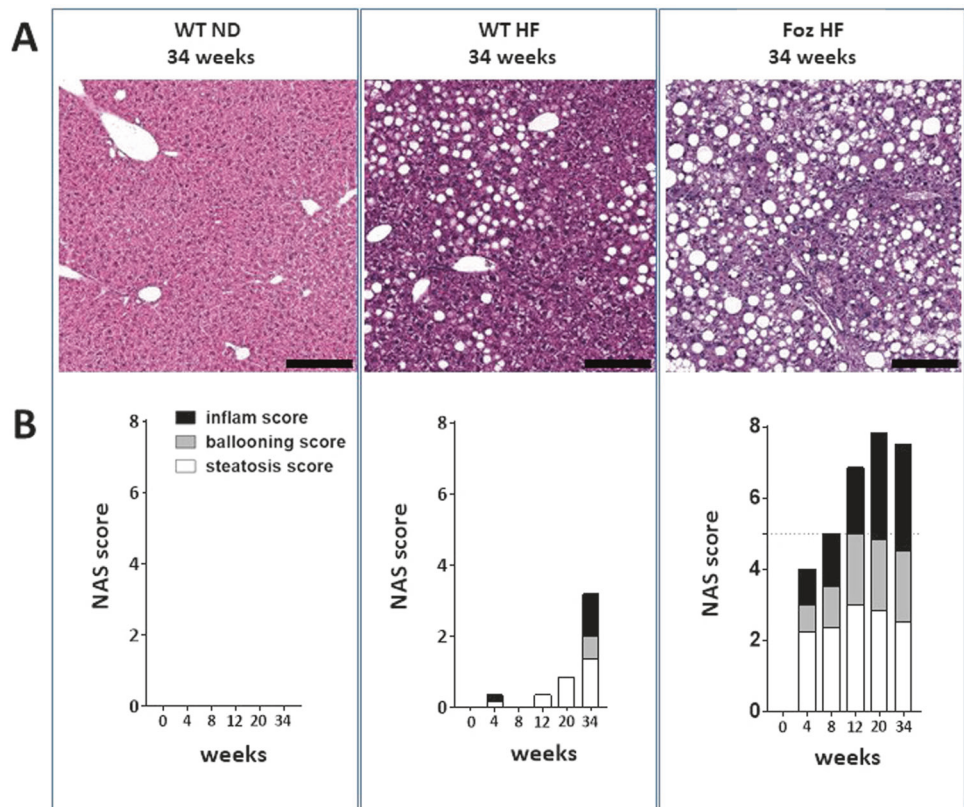
quantification and continuous variables. In the present study, we report on automated computerized image analysis of NAFLD/NASH with simultaneous quantification of steatosis, lobular inflammation, and fibrosis from the entire liver sections stained with Hematoxylin and eosin (H&E), F4/80, Ly6G immunolabeling, and picrosirius red in preclinical models. Several nutritional, genetic or toxic models have been proposed to study various aspects of NAFLD [22–26] and reviewed in [27]. The *foz/foz* mouse model is relevant model for NASH: *Foz/foz* mice voluntarily overeat and when offered a high-fat (HF) diet develop consistently a full blow NASH with fibrosis in a context of obesity-related insulin resistance and adipose tissue inflammation [28–30], while a similar dietary regimen causes progressive obesity and mild (uncomplicated) steatosis in wild-type (WT) mice. Liver pathology in *foz/foz* mice has been reviewed by experienced liver pathologists and meets the histological criteria of human NASH [28, 30, 31] including hepatocyte ballooning and presence of crown-like structures (CLS) of macrophages surrounding lipid-laden hepatocytes [32, 33]. Mild to moderate fibrosis (generally stages 1–2) develops at late stages with bridging fibrosis (F3) or cirrhosis (F4) being uncommon as in many other mouse models of NASH [27]. The *foz/foz* model has been reproduced in several laboratories [30, 33–35] and used as a preclinical model to test therapeutic interventions [32, 36–39]. C57Bl6J mice fed an HF choline-deficient diet is a model of histologically severe steatohepatitis. Metabolic syndrome and hepatocellular ballooning are however absent and therefore is not *stricto sensu* a model of NASH [27, 40–43]. In these models, we validated the accuracy of the computerized analysis to automatically assess and quantify pathological criteria versus semiquantitative scoring and biochemical investigations.

Materials and methods

Animals

NOD.B10 *foz/foz* (*Foz*) mice and their WT littermates were bred and housed in a temperature- and humidity-controlled environment in a 12-h light/12-h dark cycle. Animals had free access to food and water at all times. After weaning (time 0), male WT and *Foz* mice were fed an HF diet (OpenSource Diets D12492; 60% of calories from fat and 0.03% cholesterol) (WT HF and *Foz* HF, respectively); WT mice fed a rodent chow (WT ND) (SAFE A03 diet; 13.5% of calories from fat) served as controls. C57Bl6/J mice were fed a fat-rich choline-deficient amino acid defined (CDAA—Research Diets, A06071302) or the same diet supplement in choline (CSAA—Research Diets, A067071306) for the controls. Body weight, glycemia, and food intake were recorded once a month during the study protocol and the

Fig. 1 Histological assessment of NAFLD/NASH severity in WT and *foz/foz* mice fed an HFD. **a** Representative images of H&E-stained histological slides of WT ND, WT HF, and *Foz* HF mice at week 34 (scale bar: 200 μ m). **b** Histological NAS score [2] within each group and time point. The height of the bars corresponds to the mean NAS, the white part of the bar to steatosis score, the grey part of the bars to the ballooning score, and the black part of the bars to the inflammatory score. ($n = 5$ mice/group/time point)



liver was analyzed at time 0 and after 4, 8, 12, 20, and 34 weeks of the nutritional experiment in the *Foz* model and after 4 and 8 weeks in the CDAA model ($n = 5$ per group). At the time of kill, between 10.00 A.M. and 01.00 P.M., the liver was excised, weighted, and liver wedges snap-frozen and stored at -80°C until analysis. Wedges of the median and left lateral lobes were fixed in 4% buffered formaldehyde solution for histology purposes. The animals were handled according to the guidelines for humane care for laboratory animals established by the Université catholique de Louvain as per European Union Regulations. The local ethics committee approved the study protocol (2016/UCL/MD/003).

Liver histology

H&E staining on 5 μ m thick sections of paraffin-embedded livers was used for routine histological evaluation and assessment of NAS score according to Kleiner et al. [2], as previously done for assessment of NAFLD severity in this mouse strain [38]. Picrosirius red staining was performed to assess fibrosis. For immunohistochemical detection of F4/80, paraffin sections were treated with proteinase K, exposed to a primary rat anti-mouse F4/80 monoclonal antibody (1/200) (MCA497G, BioRad). For the detection of Ly6G, slides were immersed in EDTA pH8 at 95°C for 30 min for antigen retrieval, and then exposed to a primary rat anti-mouse Ly6G

Ab (1/2000) (DB Pharmingen 551459). A rabbit anti-rat immunoglobulin (1/200) (AI-4001, Vector) is then applied followed by a goat anti-rabbit streptavidin horseradish peroxidase-conjugated antibody (K4003 EnVision, Dako). The peroxidase activity was revealed with diaminobenzidine and slides were counterstained with hematoxylin.

Automated histological analysis

All tissue sections used for the automatic assessment of NAFLD/NASH were scanned at $\times 20$ using a NanoZoomer-SQ. Digital images of entire liver sections were captured using the NDP.view 2 software (both from Hamamatsu Corporation, Hamamatsu, Japan). The quantification of steatosis, inflammation, and fibrosis was carried out on three entire liver sections per animal and five animals per group thanks to dedicated image processing software developed by Biocellvia. Macrosteatosis was assessed on H&E-stained slides. The software solution allows accurate discrimination of empty vesicles (size $> 10 \mu\text{m}^2$) contained in the entire liver sections and automatically discard the main vessels and large empty space. This program assesses automatically the number and the area of vesicles scattered in the entire liver section from the native RGB image (pixel size: 0.452 μm). The percentage of steatosis is calculated based on the total area of vesicles versus the area of the liver section. The mean size of vesicles was computed as the ratio

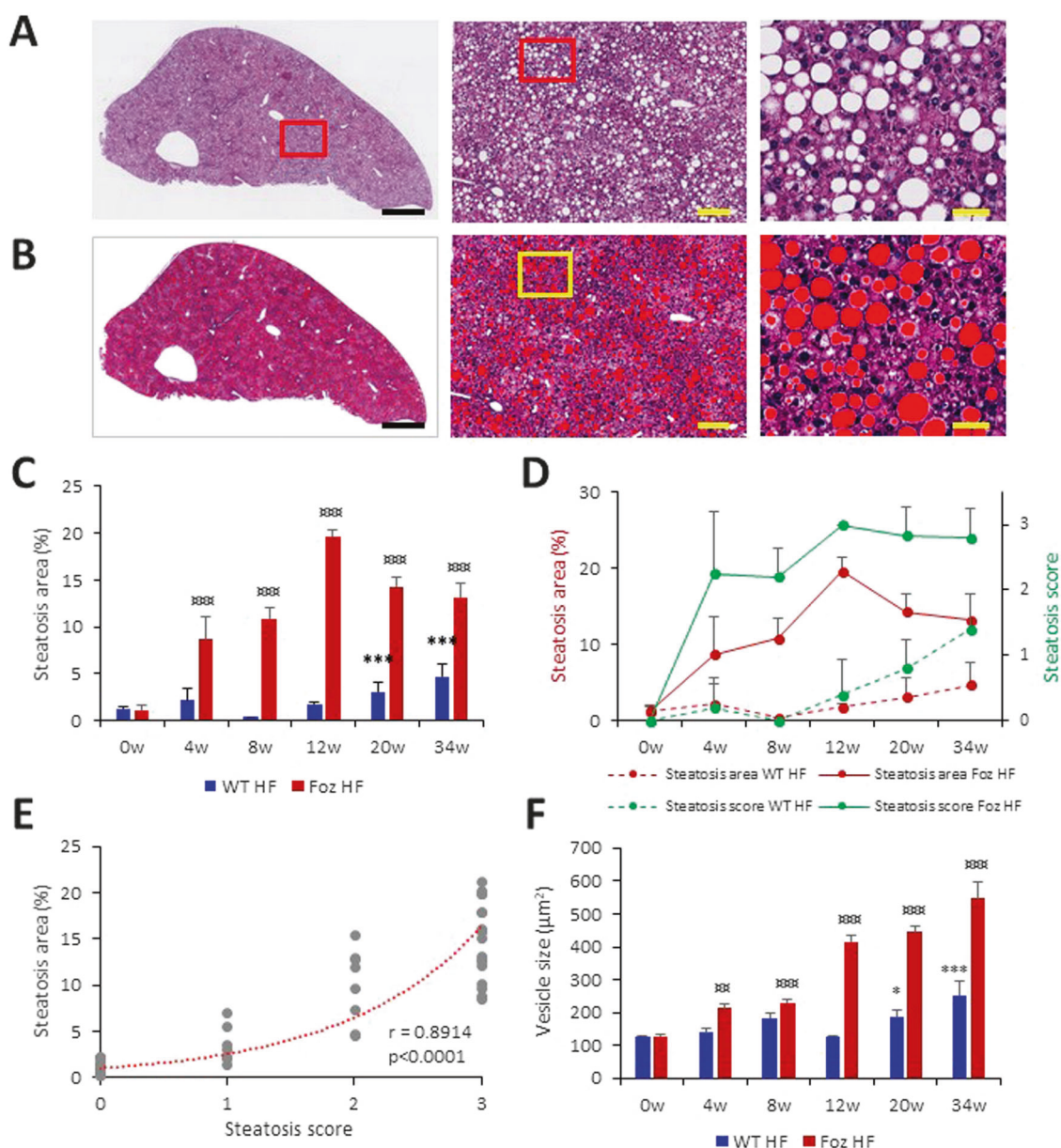


Fig. 2 **a** Representative native image of the Foz HF liver section stained with H&E at week 12. **b** Biocellvia software discrimination of macrovesicles showed in native image **a** in which macrovesicles were pseudo colored in red (Scale bars **a**, **b**: left: 1 mm; middle: 220 μm ; right: 35 μm). **c** Evolution of steatosis area relative to selected time points in WT HF and Foz HF mice. **d** The comparison between steatosis area and steatosis score relative to selected time points in WT HF and Foz HF mice. **e** The correlation between steatosis area and

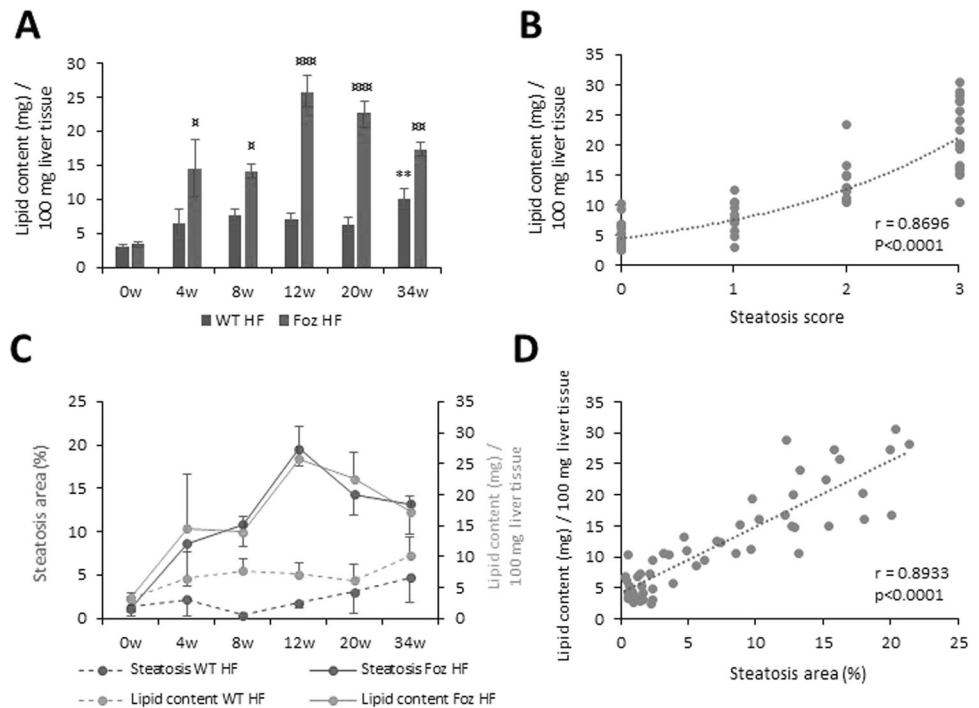
steatosis score assessed in WT HF and Foz HF mice. **f** Evolution of the mean fat vesicle size (μm^2) relative to selected time points in WT HF and Foz HF mice. The asterisk denotes the comparison of WT HF to WT HF at week 0; * $p < 0.05$, *** $p < 0.001$. The currency symbol denotes the comparison of Foz HF to Foz HF at week 0; $\text{¤¤¤}p < 0.01$, $\text{¤¤¤¤}p < 0.001$. $r =$ Spearman coefficient. Results were expressed as the mean value per group \pm SD ($n = 5$ mice/group)

of total vesicle area versus the total number of vesicles. In NASH, the aggregation of active macrophages around fat-laden hepatocytes (CLS) correlates with liver inflammation and fibrosis [44]. F4/80 immunopositive CLS were discriminated automatically in the entire liver section and their number expressed per mm^2 . Ly6G immunolabeling was expressed as the % Ly6G positive area in the entire liver section. The analysis of fibrosis was performed on entire

liver sections stained with picrosirius red. A software automatically delineated tissue area and segmented the Sirius red-stained collagen fibers. Fibrosis was expressed as the ratio of the area of stained collagen fibers versus the area of the liver section in %.

Detailed methodology for biochemical quantification of lipids, gene expression analysis, and micro-computed tomography analysis is provided in the supplementary material.

Fig. 3 **a** Evolution of lipid content relative to selected time points in WT HF and Foz HF mice. **b** The correlation between liver lipid content and steatosis score assessed in WT HF and Foz HF mice. **c** The comparison of steatosis area and liver lipid content assessed in WT HF and Foz HF mice at selected time points. **d** The correlation between liver lipid content and steatosis area assessed in WT HF and Foz HF mice. The asterisk denotes the comparison of WT HF to WT HF at week 0; $**p < 0.01$. The currency symbol denotes the comparison of Foz HF to Foz HF at week 0; $\$p < 0.05$, $\$\$p < 0.01$, $\$\$\$p < 0.001$. r = Spearman coefficient. Results were expressed as mean value \pm SD ($n = 5$ mice/group)



Statistical analysis

Data are presented as mean \pm standard deviation. Statistical differences between groups were analyzed using Student's *t*-test or one-way analysis of variance with subsequent Dunnett's multiple comparison test for all parametric data and Kruskal–Wallis test followed by Dunn's multiple comparison test for nonparametric data (GraphPad Prism 8.0; GraphPad Software, Inc. La Jolla, CA). Spearman correlation coefficient has been calculated to determine the statistical significance of correlated data. A *p*-value of < 0.05 was considered statistically significant.

Results

Foz HF mice exhibit progressive NASH and WT HF simple steatosis

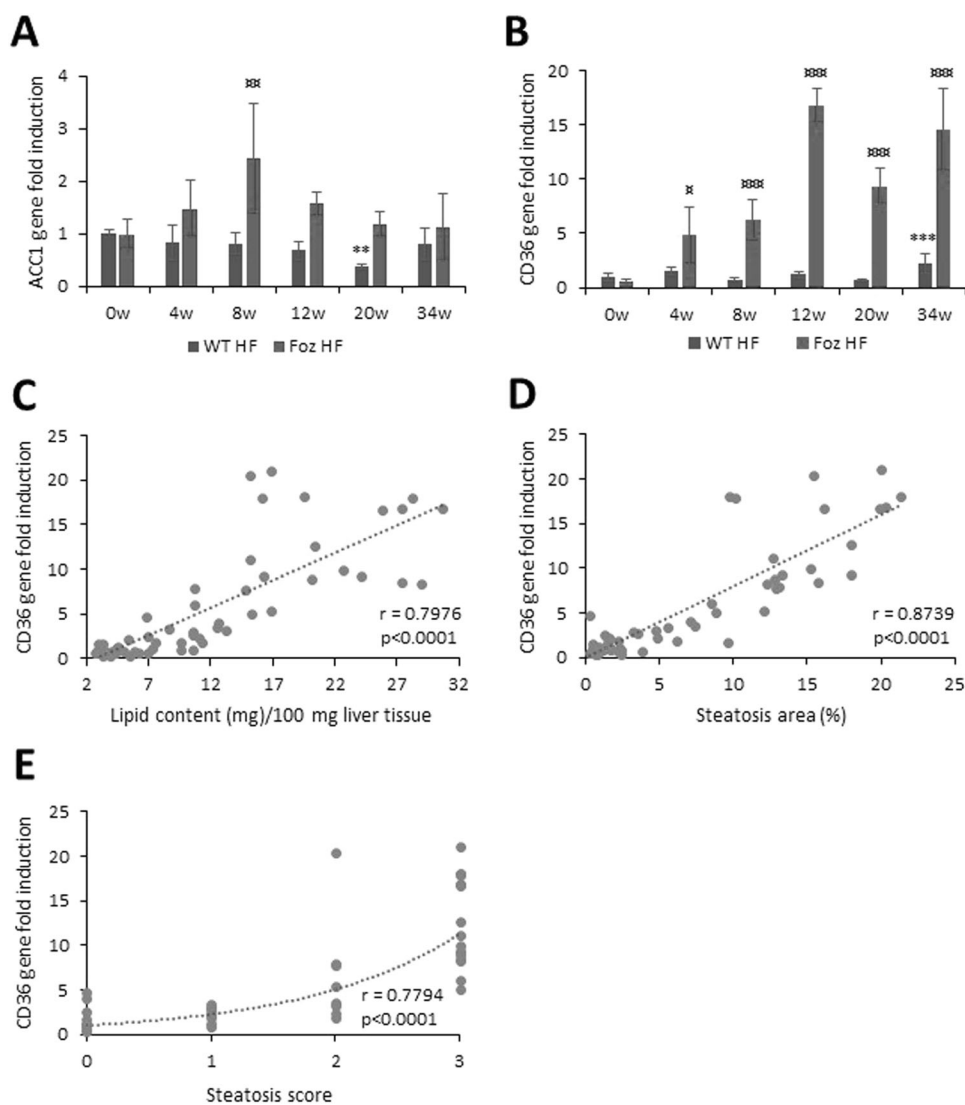
WT mice on an ND have normal liver histology. On an HF diet, they develop moderate steatosis at the late time point of the feeding experiment (34 weeks). By contrast and in accordance with previous reports [28, 31, 38], Foz HF develop rapidly a pan lobular macrosteatosis with ballooning and inflammation (Fig. 1a). As defined per Kleiner et al. [2], most Foz HF mice had a NAS score > 5 (the NASH defining limit) at 8 weeks and all mice in the group reached the maximum score of 8 at 20 weeks (Fig. 1b). The steatosis score increased first, followed by ballooning and inflammation scores together. In WT HF mice, mild steatosis

(score ≤ 2) developed with minimal inflammation and rare ballooning at week 34 (Fig. 1b). Anthropometric data are provided in Supplementary Fig. 1.

Automated quantification of steatosis area highly correlates with steatosis scoring

The automated quantification of steatosis is based on the recognition at high magnification (pixel size $0.452 \mu\text{m}$) of the round, empty vesicles with a size $> 10 \mu\text{m}^2$ on H&E-stained liver sections. The steatosis area (%) corresponds to the ratio of the sum of vesicle area and the total area of the liver section, the large vessels and empty spaces being automatically discarded from the analysis (Fig. 2a, b). The analysis performed on control livers without steatosis (WT and Foz 0 W) indicated that the identification of small vessels (false positive) corresponded to $< 1.5\%$ of the liver area (Fig. 2c). To evaluate the performance of the software to quantify steatosis, we compared software output with standard histological scoring. In *foz/foz* mice, HFD induced a gradual and significant increase of steatosis area as early as week 4 to reach a maximum value at week 12 (Fig. 2c). In WT HF mice, steatosis developed at a much lesser extent (3–5 times lower) and later time points (weeks 20 and 34) (Fig. 2c). Computed steatosis area paralleled steatosis scores (Fig. 2d) with a spearman rank correlation of 89.1% (Fig. 2e). At week 12, all FOZ HF had the maximum steatosis score of 3, which corresponds to 20% of the area of the liver section being occupied by lipid vesicles. The mean size of lipid vesicles

Fig. 4 Evolution of **a** ACC1 and **b** CD36 gene expression relative to selected time points in WT HF and Foz HF mice. The correlation between CD36 gene expression and **c** total lipid content, **d** steatosis area, and **e** steatosis score assessed in WT HF and Foz HF mice. The asterisk denotes the comparison of WT HF to WT HF at week 0; $**p < 0.01$, $***p < 0.001$. The currency symbol denotes the comparison of Foz HF to Foz HF at week 0; $*p < 0.05$, $**p < 0.01$, $***p < 0.001$. $r =$ Spearman coefficient. Results were expressed as mean value \pm SD ($n = 5$ mice/group)



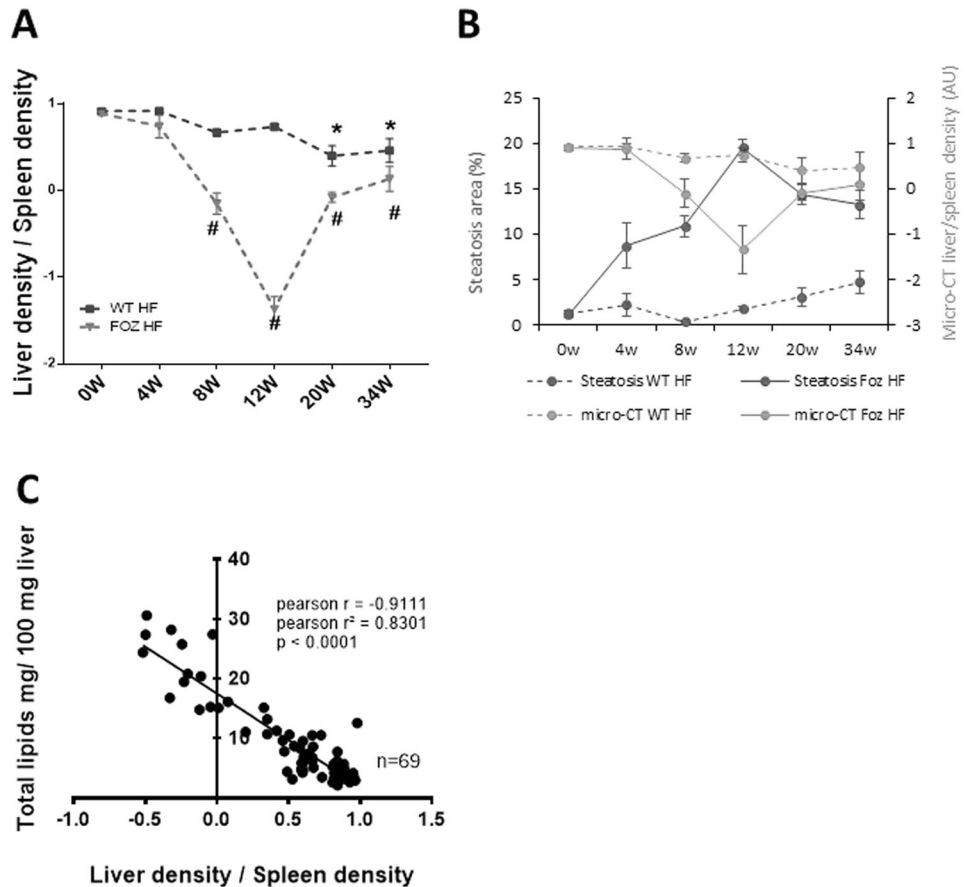
gradually and significantly increased with steatosis severity (Fig. 2f).

Automated assessment of steatosis area is coordinated positively with lipid content

We quantified liver lipids by a biochemical method. Control livers contained < 3.5 mg lipids per 100 g liver. A gradual and significant increase of liver lipid content was observed with the duration of HF feeding reaching a maximum value at week 12 in Foz HF (Fig. 3a) while it was significant only at week 34 in WT HF. The mean lipid content as assessed biochemically increased accordingly to the histological steatosis score (Fig. 3b, spearman rank correlation of 87%). In Foz HF mice, automatically assessed steatosis area perfectly matched liver lipid content but slightly underestimated it in WT HF possibly due to the presence of very small vesicles not integrated by the automated image

analysis (Fig. 3c). In the entire WT HF and Foz HF cohorts, steatosis area highly correlated with biochemical lipid content (Fig. 3d, spearman rank correlation of 89.3%). We then analyzed the expression of key genes involved in lipid uptake (CD36), de novo lipogenesis (ACC1, FAS, and SCD1) and β -oxidation (ACO). In Foz HF mice, steatosis was associated with an early increase in ACC1 mRNA up to week 8 (Fig. 4a) and with a large increase in CD36 mRNA at all investigated time points (Fig. 4b); ACO mRNA, moderately increased at weeks 4, 8, and 12, while expression of SCD1 mRNA and FAS mRNA was stable over time (Supplementary Fig. 2). In WT HF, there was no patent change in the expression of these genes over time. Overall, the present results suggest that, in Foz HF mice, increased fatty acid uptake predominantly contributes to steatosis. In support, hepatic expression of the up-take transporter CD36 correlated with lipid content (Fig. 4c), steatosis area (Fig. 4d), and steatosis score (Fig. 4e).

Fig. 5 **a** Liver-to-spleen density in WT and FOZ HF along the study period. **b** The comparison between the steatosis area obtained by automated analysis of histological H&E-stained liver sections and liver/spleen micro-CT density relative to selected time points in WT HF and Foz HF mice. **c** The correlation between liver total lipid content assessed by the biochemical assay and liver/spleen density obtained by CT-scan. The asterisk denotes a statistical difference in WT HF versus control (time 0) and the hash symbol in FOZ HF versus control (time 0)



Comparison of steatosis area with liver tissue density assessed by micro-CT analysis

Currently, 20–33% is considered a reliable level at which steatosis is detected by imaging methods, such as CT-scan in humans [10]. However, the presence of fat >5–10% is considered abnormal. CT-scan data are scarce in preclinical models [45, 46]. We, therefore, analyzed liver density by CT-Scan in our cohort. The liver density was significantly lower in WT HF at 34 weeks and in the Foz HF at 8 weeks (Fig. 5a), timings at which liver lipid contents were 10% and 15%, respectively. Changes of liver tissue density perfectly mirrored those of steatosis area (Fig. 5b) and strongly correlated with liver lipid content (Fig. 5c).

Comparison of histological inflammatory scores with automatic quantification of hepatic macrophage crown-like structures

In Foz HF mice, progression to NASH was associated with an early and gradual increase of F4/80 mRNA which was not observed in WT HF mice (Fig. 5d). In Foz HF, macrophage CLS surrounding hepatocytes with large macrovesicles were present as early as week 4 (Fig. 6a) and much

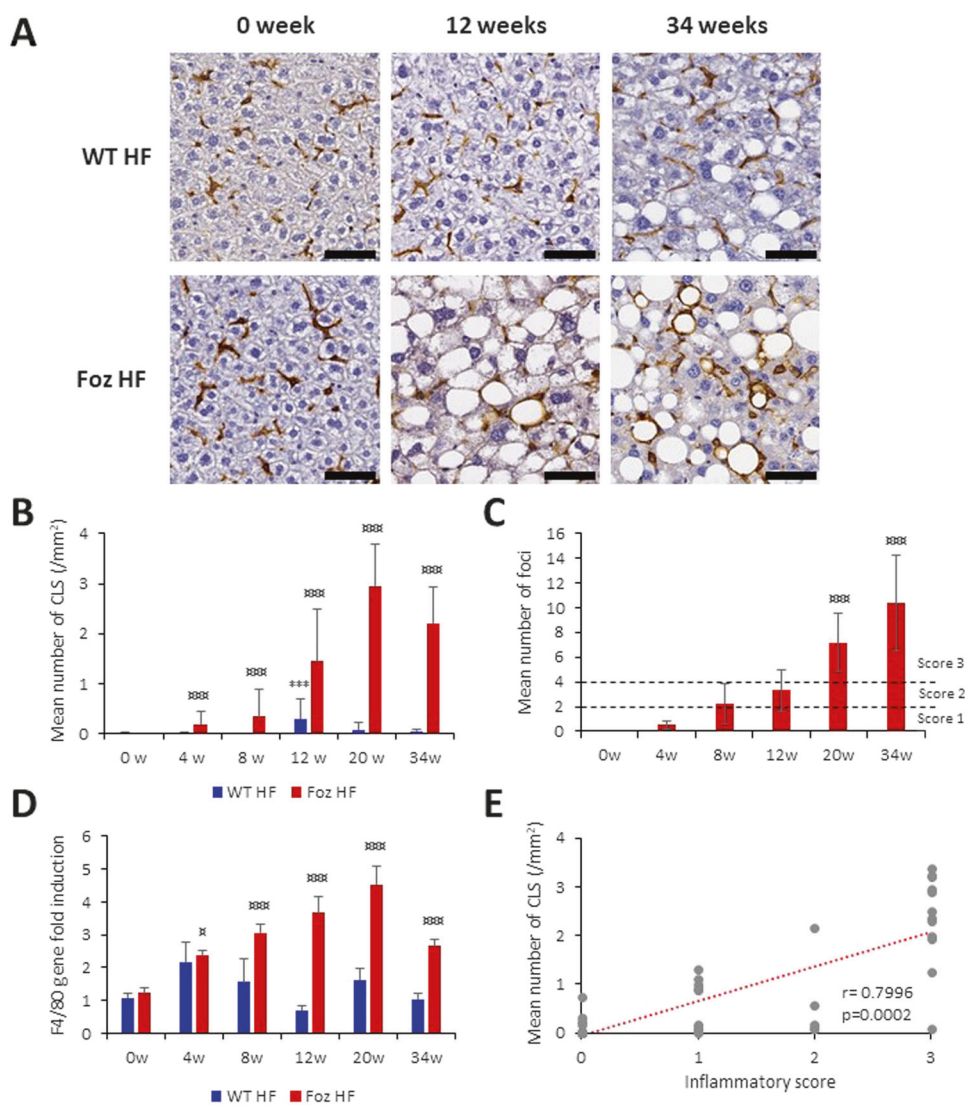
more numerous as diseases progresses. CLS were automatically detected by pattern recognition on F4/80 immunostained sections. The number of CLS, automatically assessed, gradually increased with a maximum at week 20 (Fig. 6b) in Foz HF. In WT HF mice the presence of CLS was automatically captured only at week 12. The evolution of CLS number with time is in agreement with that of histologically defined inflammatory scores (Fig. 6c): In Foz HF mice, the number of inflammatory foci per high ($\times 20$) power field determine by visual analysis and thus the inflammatory score [2] increased continuously with time (Fig. 6c). It should be emphasized that in week 4 samples characterized by a $NAS_{inflammation}$ at 1, the number of CLS was already increased. Inflammatory score and macrophage CLS presented a high Spearman rank correlation of 80% (Fig. 6f). The Ly6G positive area, a surrogate for neutrophil infiltration, did not vary significantly during disease progression (Supplementary Fig. 3).

Fibrosis assessment

As revealed by the histological evaluation of picrosirius red-stained sections, Foz HF exhibited pericellular fibrosis at week 20, with fibrosis substantially progressing at week 34.

Fig. 6 **a** Representative native images of F4/80-immunostained liver sections at weeks 0, 12, and 34 in WT HF and Foz HF mice; note the formation of crown-like structure (CLS) in Foz HF mice at week 12 and 34 (scale bars: 55 μm). **b** Evolution of the number of CLS/ mm^2 of liver tissue in WT HF and Foz HF mice relative to selected time points. **c** Evolution of the mean number of inflammatory foci (mean number/group) and corresponding inflammatory scores in Foz HF mice at selected time points.

Supplementary statistics:
4 weeks/20 weeks $p = 0.001$,
4 weeks/34 weeks $p < 0.0001$,
12 weeks/34 weeks $p = 0.0005$.
d Evolution of F4/80 gene expression in WT HF and Foz HF mice relative to selected time points. **e** The comparison between the evolution of the number of CLS and inflammatory score in WT HF and Foz HF mice. The asterisk denotes the comparison of WT HF to WT HF at week 0; *** $p < 0.001$. The currency symbol denotes the comparison of Foz HF to Foz HF at week 0; $p < 0.05$, $\text{¤¤¤}p < 0.001$. Results were expressed as mean value \pm SD ($n = 5$ mice/group)



There was no fibrosis in WT HF (Fig. 7a). In WT HF, there is no change over time in total collagen content determined by automated segmentation and quantification of digital images of picrosirius red-stained sections (Fig. 7b) nor in the expression of collagen 1 α 1 gene (Fig. 7c). In Foz HF, total collagen content as automatically assessed, significantly increased from week 20 reaching a value three times higher at week 34 (Fig. 7b). The expression of mRNA collagen 1 α 1 increased as early as week 4 showing that fibrogenic processes are engaged early in NASH pathogenesis, well before collagen deposition (Fig. 7c). Several enzymes are involved in extracellular matrix remodeling, mainly MMP-2,-9 (not shown), MMP13 and TIMP1. MMP13 and TIMP1 gene expression levels were significantly induced in Foz HF with a maximum tenfold induction at week 12 compared with WT HF (Fig. 7d, e). Thereafter, TIMP1 gene expression, but not MMP13, further increased, giving rise at week 20 to a large excess of

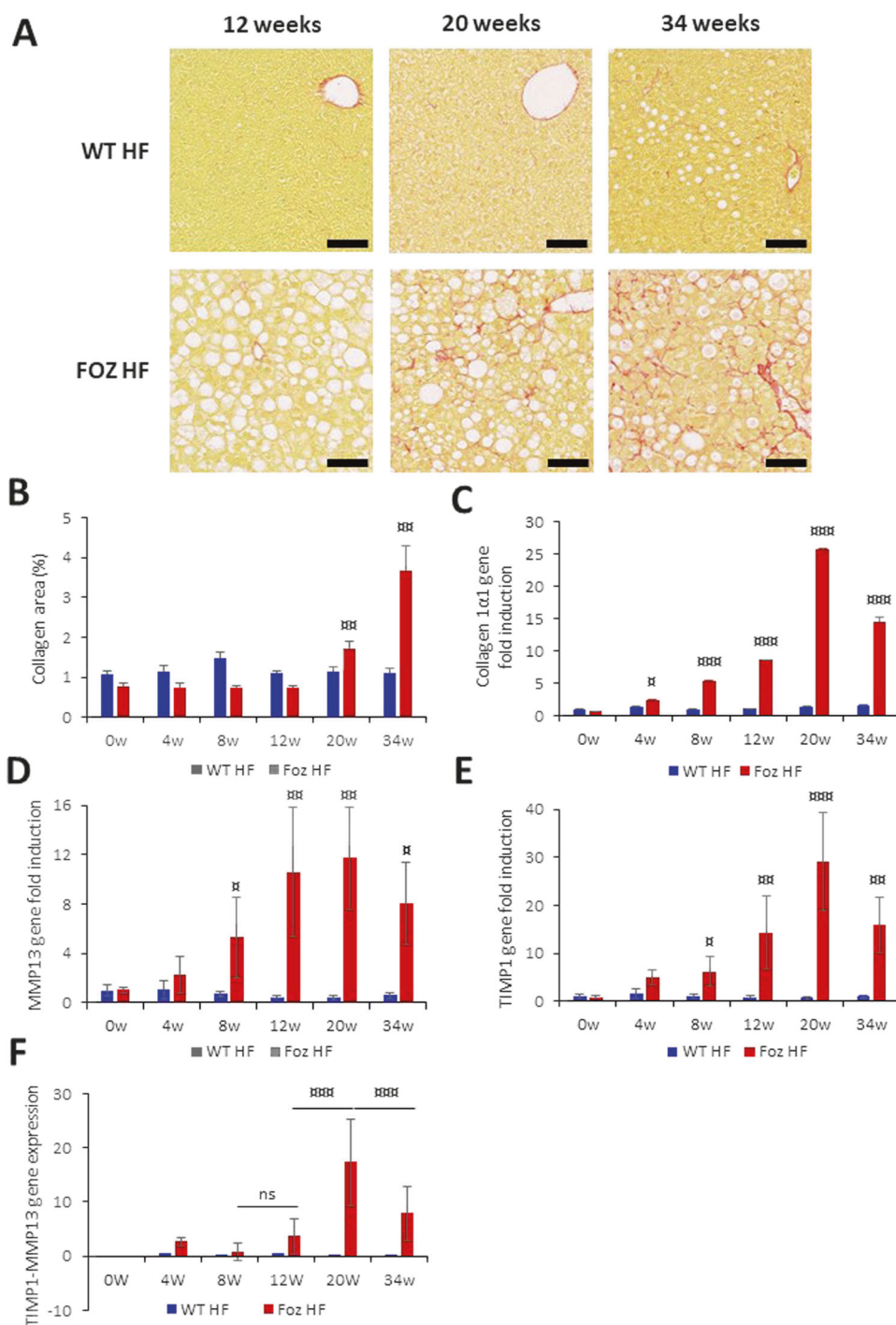
TIMP1 over MMPs leading very likely to a decrease of remodeling and scar matrix accumulation (Fig. 7f).

The comparison of the evolution of collagen deposition and inflammation whether determined by histological scoring or by computerized analysis showed a clear temporal dissociation: inflammation developed early and gradually while collagen deposition occurred much later (Fig. 8a, b). There is no association between steatosis and collagen deposition (Fig. 8c).

Application of the automated procedure for quantification of steatosis, inflammation, and fibrosis in an independent model

We applied the developed methodology for the quantification of NAFLD criteria in an unrelated model of steatohepatitis, namely mice fed a fat-rich diet deficient in choline. Choline deficiency inhibits VLDL secretion while the HF

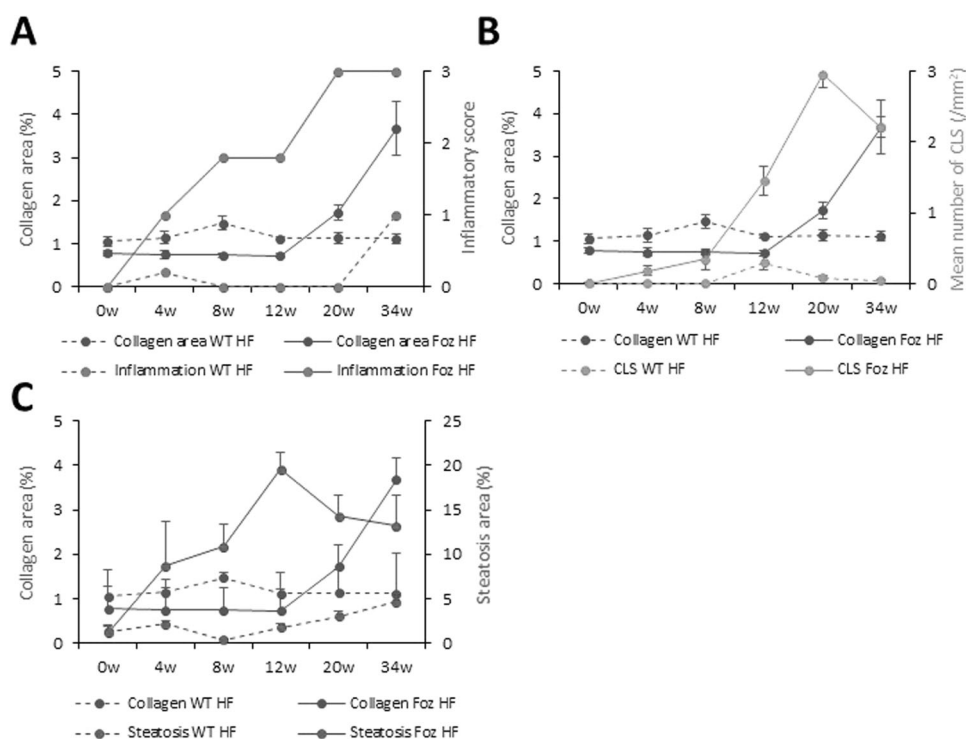
Fig. 7 a Representative native images of picrosirius red-stained liver sections from WT HF and Foz HF mice at weeks 12, 20, and 34 (scale bars: 100 μ m). **b** Evolution of collagen area assessed by digital analysis from WT HF and Foz HF mice relative to selected time points. Evolution of **c** collagen α 1, **d** MMP13, **e** TIMP1 gene expression in WT HF and Foz HF mice relative to selected time points. **f** Histogram of differences between TIMP1 and MMP13 gene expression relative to selected time points (12 weeks/20 weeks $p < 0.0001$, 20 weeks/34 weeks $p < 0.0001$). The currency symbol denotes the comparison of Foz HF to Foz mice at week 0; $\#p < 0.05$, $\#\#p < 0.01$, $\#\#\#p < 0.001$; ns nonsignificant. Results were expressed as mean value \pm SD ($n = 5$ mice/group)



content prevents the weight loss that results from choline deficiency [27, 40–43]. Severe predominantly macrovesicular steatosis (NAS steatosis = 3), severe mixed inflammation (NAS inflammation = 3), and fibrosis (Fig. 9) were faithfully captured and quantitated by the automatic procedure (Fig. 10 a–d). Note that phagocytic macrophages and neutrophils are part of the prominent inflammation seen in this model (Fig. 9). The confluence of inflammatory foci (Fig. 9) precluded precise counting. The number of F4/80

CLS was four times higher than in the Foz model (Fig. 10b vs Fig. 6b). The Ly6G positive area significantly increased with the duration of the feeding experiment (Fig. 10c), while this criterion was inconstant and did not reliably reflect the severity of inflammation in the Foz model (Supplementary Fig. 3). As for the Foz model, the fine pericellular fibrosis and its evolution over time were captured by automated assessment of collagen deposition in the entire liver section (Fig. 10d).

Fig. 8 The comparison between the evolution of collagen area and **a** inflammatory score, **b** the number of CLS/mm² of liver tissue and **c** steatosis area in WT HF and Foz HF mice relative to selected time points. Results were expressed as mean value \pm SD ($n = 5$ mice/group)



Discussion

The automated computerized image analysis developed in the present study shows that a faithful and fast quantification of the severity of NAFLD/NASH, totally independent of the experimenter evaluation, can be accessed from a continuous measure of its key histological features: steatosis, inflammation, and fibrosis.

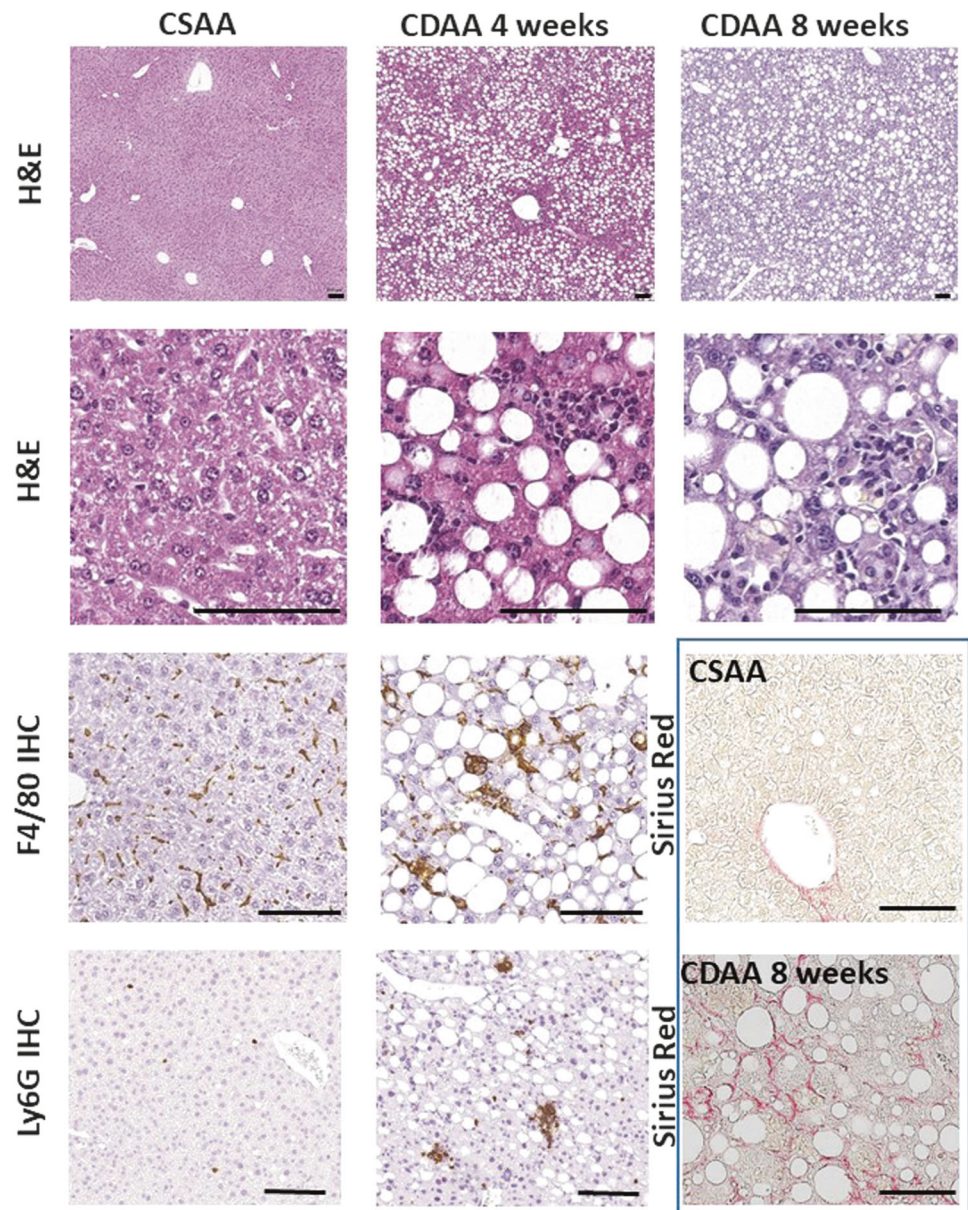
The automated quantification of steatosis based on the measure of the macrovesicle area highly correlated with the established steatosis scores performed on the same liver sections ($r = 0.89$) in agreement with that found in other computerized imaging studies carried out with diverse software's [47–52]. Some empty vascular spaces may be mistaken as lipid vesicles thus overestimate steatosis level. The analysis we performed on nonsteatotic livers indicated that the identification of sinusoids corresponded to less than 1.5% of the liver area, i.e., 7.6 and 17.4 fold lesser than steatosis area recorded in mild and severe steatosis in Foz HF. The high correlation with steatosis score and lipid content also supports that the identification of “white spaces” has a negligible effect on the assessment of steatosis area. The observation that the time course of the increase of steatosis area index perfectly matches that of lipid content but not the steatosis score based on the percentage of fatty hepatocytes further support that a continuous variable such as obtained by the automate histological measure better reflects lipid content than the histological categorical score. This strengthens the potential value of steatosis area index

as an operator-independent and accurate readout of macrosteatosis.

Besides, computerized image analysis enables to quantify the size of the lipid vesicles. We showed for the first time that the mean size of the vesicles correlated positively with the increase of steatosis during disease progression in Foz HF. In this particular mouse model, steatosis severity is contributed to by the increased proportion of hepatocytes bearing lipid droplets (a parameter captured by the steatosis score) and by the increased size of lipid vesicles. Therapeutic interventions in preclinical models that achieve steatosis reduction unanimously also show a reduction in vesicles' size [31, 32, 39]. Therefore, it is tempting to speculate that monitoring of the vacuoles' size could indicate steatosis evolution and inform on progression or regression in advance of the gain or loss of one point of steatosis score. This is of particular interest to shorten preclinical studies for antisteatosis drug screening. Determination of droplet size is also an important criterion in liver transplantation as the presence of large fat droplets in more than 30% of hepatocytes is a risk factor for primary non-function, mortality, and morbidity. Nativ et al. suggested that automated analysis of droplet size and nucleus displacement might help to standardize the criteria for assessing the transplantability of NAFLD livers [16].

The relative liver tissue density assessed noninvasively by micro-CT-scan accurately detects changes in liver lipid contents with a threshold around 10% offering an alternative to MRI PDFF for noninvasive quantification of

Fig. 9 Representative histological image of liver sections of mice fed the CSAA or the CDAA diet for 4 and 8 weeks and stained: H&E staining (low and high magnification), F4/80 and Ly6G immunostainings and Sirius red staining are presented. (Scale bars: 100 μ m)

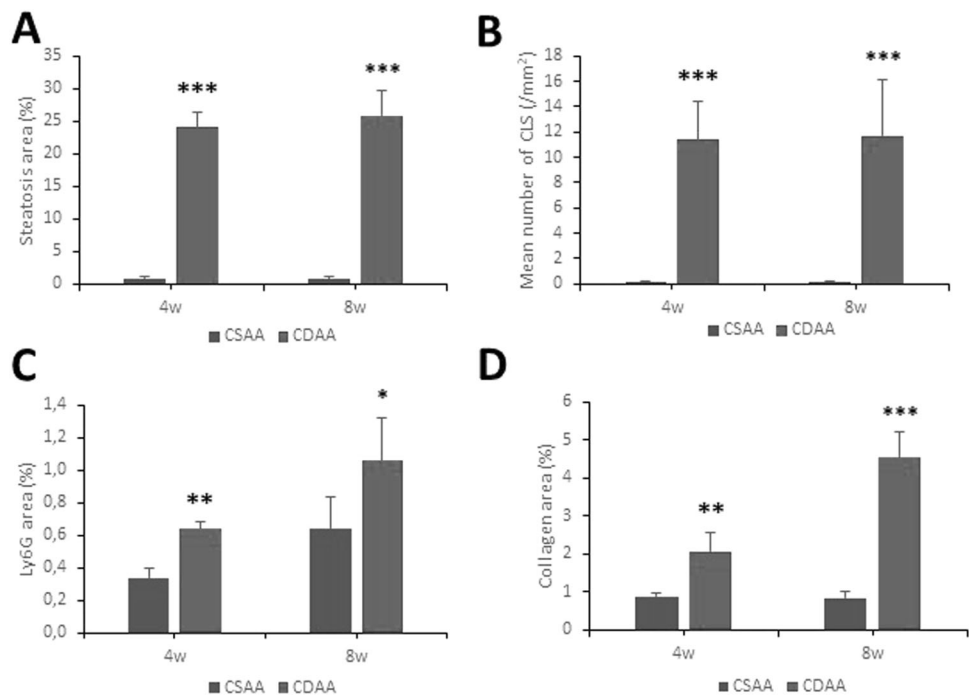


steatosis in preclinical models [53]. Possible explanations for higher sensitivity for steatosis detection with micro-CT in mouse than in human studies are the higher voxel resolution and the larger volume of interest relative to the liver volume on which density is measured.

The automated quantification of CLS macrophages represents a robust tool to quantitate accurately and reliably NASH-associated inflammation, totally independent of the experimenter, in other words without any intra- and inter-observer variability. Macrophages are involved in the pathogenesis of NASH induced experimentally in rodents following long term HFD feeding [44, 54, 55]. Active macrophages indeed aggregate around fatty hepatocytes to constitute the so-called CLS [31, 44]. Unlike resident macrophages and immune cells, CLS macrophages were strictly absent in

control livers and livers with simple steatosis such as in WT HF mice [31, 44]. The number of CLS immunolabeled with F4/80 gradually and significantly increased in parallel with disease severity in the *foz* HF model as also reported in HFD-fed melanocortin-4 receptor-deficient (MC4R-KO) mice [44]. In *Foz* HF, the number of CLS macrophages correlates with the inflammatory score. The link between CLS macrophages and inflammation processes is also highlighted by the fact that in *foz/foz* mice amelioration of NASH severity with pharmacological treatments leads to a disappearance of CLS [31]. In CDAA livers, the number of CLS was similar at the 2 time points examined although disease severity and fibrosis increased. In this model with severe inflammation, monitoring the recruitment of neutrophils into the inflammatory foci appears of greater value to monitor disease progression.

Fig. 10 **a** Steatosis area, **b** the number of F4/80 positive CLS, **c** Ly6G immunopositive area and **d** quantification of collagen deposition as assessed by digital analysis in mice fed the CSAA or the CDAA diet for 4 and 8 weeks. * $p < 0.05$, ** $p < 0.01$, *** $p < 0.001$ in CDAA versus CSAA at the respective time points



In Foz HF mice, scar collagen was only detected after 20 weeks of HFD treatment, although the fibrotic process, assessed by the expression of mRNA collagen 1 α 1, was activated as soon as week 4. Collagen starts accumulating when the concomitant fibrolysis processes are inhibited [56, 57]. Our data indicated that in Foz HF mice, inflammation and steatosis processes largely preceded the expression of fibrosis. These findings underline the importance of knowing the evolution of fibrosis in a given experimental model in view to define precisely the optimum test window for evaluating the effectiveness of new therapeutic molecules. In the present study, fibrosis was quantified in the entire liver section for determining the total content of collagen regardless of its distribution in perisinusoidal, central vein and portal zone. Further developments are needed to obtain a fully automatic (observer-independent) analysis of the zonal distribution of collagen depots.

The automated computerized image analysis developed in the present study provides an accurate and very rapid assessment of the severity of NAFLD/NASH by quantifying concomitantly the macrosteatosis, inflammation, and fibrosis. Although these key NAFLD/NASH parameters were analyzed sequentially from three entire and serial liver slides, their quantitative analysis is not done at the expense of computing time since it is reduced to a minute per liver section (2 h per 100 liver sections). Investigations are in progress to realize at least macrosteatosis and inflammation from digital data from a unique liver section. The enormous advantage of the digital method is that it is fully automatic and, for all steps from scan recording to statistical analysis, experimenter-independent.

Also, criteria for detection and quantification are strictly identical for all samples examined, enabling valid comparison and standardization. Moreover, the system is versatile and allows to tailor the parameters of interest according to the specific pathological features of the NAFLD model.

Other investigations are required to discriminate and reliably quantify hepatocyte ballooning. Ballooning is evident in Foz HF livers (Supplementary Fig. 4). The definition of criteria for defining ballooning in rodents on conventional H&E-stained sections is poor and, according to our experience, inadequate for automated pattern recognition. Moreover, conversely to human pathology [58–60], the immunohistological signature of ballooned cells has not been established in rodent livers. Gene expression analysis is another approach to monitor disease evolution. However, the data sets described (e.g., in [61]) are not unique to NASH and did not make any discrimination between NASH and simple steatosis. Non-invasive methods and biomarkers, to date, may only help in identifying and quantifying steatosis and for the diagnosis of severe fibrosis. Therefore, at this point, the histological assessment remains the most reliable method to assess NASH. The computerized procedure frees the acquisition of the parameters from a possible observer's bias. The generation of quantitative values and the addition of parameters such as the lipid vacuole size increase the accuracy for the assessment of disease evolution and regression. If proved powerful and robust to evaluate the impact of therapeutic manipulation in preclinical models, this will pave the way for the development of similar automated image analysis procedures for the monitoring of disease evolution on human biopsies.

Funding This work is supported by a grant from the Fund for Scientific Medical Research (FRS-FNRS, Belgium, PDR T.0141.19); MN is the recipient of a Ph.D. fellowship from FRIA (FNRS, Belgium). YJ is the chief scientific officer of Biocellvia, Marseille, France.

Author contributions MDR, MN, and HL performed the animal experiments, prepared the material, performed biochemical, and gene expression analyses. CB performed the quality control on images used for analyses. CB, YJ, and IAL designed the study and analyses. MDR optimized the histological stainings. MN and GVV acquired and analyzed micro-CT data. MDR, MN, YJ, and IL critically reviewed and analyzed the data. MDR and YJ prepared the figures. MDR, YJ, and IAL prepared the manuscript. All authors read and revised the manuscript.

Compliance with ethical standards

Conflict of interest YJ is the chief scientific officer of Biocellvia, Marseille, France. The other authors declare that they have no conflict of interest.

Publisher's note Springer Nature remains neutral with regard to jurisdictional claims in published maps and institutional affiliations.

References

- Arab JP, Arrese M, Trauner M. Recent Insights into the pathogenesis of nonalcoholic fatty liver disease. *Annu Rev Pathol.* 2018;13:321–50.
- Kleiner DE, Brunt EM, Van NM, Behling C, Contos MJ, Cummings OW, et al. Design and validation of a histological scoring system for nonalcoholic fatty liver disease. *Hepatology.* 2005;41:1313–21.
- Bedossa P. Utility and appropriateness of the fatty liver inhibition of progression (FLIP) algorithm and steatosis, activity, and fibrosis (SAF) score in the evaluation of biopsies of nonalcoholic fatty liver disease. *Hepatology.* 2014;60:565–75.
- Rinella ME, Tacke F, Sanyal AJ, Anstee QM. Report on the AASLD/EASL joint workshop on clinical trial endpoints in NAFLD. *J Hepatol.* 2019;9:S0168–8278.
- Ratziu V. A critical review of endpoints for non-cirrhotic NASH therapeutic trials. *J Hepatol.* 2018;68:353–61.
- Gawrieh S, Knoedler DM, Saeian K, Wallace JR, Komorowski RA. Effects of interventions on intra- and inter-observer agreement on interpretation of nonalcoholic fatty liver disease histology. *Ann Diagn Pathol.* 2011;15:19–24.
- Fukusato T, Fukushima J, Shiga J, Takahashi Y, Nakano T, Maeyama S, et al. Interobserver variation in the histopathological assessment of nonalcoholic steatohepatitis. *Hepatol Res.* 2005;33:122–7.
- Merriman RB, Ferrell LD, Patti MG, Weston SR, Pabst MS, Aouizerat BE, et al. Correlation of paired liver biopsies in morbidly obese patients with suspected nonalcoholic fatty liver disease. *Hepatology.* 2006;44:874–80.
- Dulai PS, Singh S, Patel J, Soni M, Prokop LJ, Younossi Z, et al. Increased risk of mortality by fibrosis stage in nonalcoholic fatty liver disease: systematic review and meta-analysis. *Hepatology.* 2017;65:1557–65.
- Castera L, Friedrich-Rust M, Loomba R. Noninvasive assessment of liver disease in patients with nonalcoholic fatty liver disease. *Gastroenterology.* 2019;156:1264–81.
- Goceri E, Shah ZK, Layman R, Jiang X, Gurcan MN. Quantification of liver fat: a comprehensive review. *Comput Biol Med.* 2016;71:174–89.
- Han MA, Saouaf R, Ayoub W, Todo T, Mena E, Nouredin M. Magnetic resonance imaging and transient elastography in the management of nonalcoholic fatty liver disease (NAFLD). *Expert Rev Clin Pharmacol.* 2017;10:379–90.
- Esterson YB, Grimaldi GM. Radiologic imaging in nonalcoholic fatty liver disease and nonalcoholic steatohepatitis. *Clin Liver Dis.* 2018;22:93–108.
- Allen AM, Shah VH, Therneau TM, Venkatesh SK, Mounajjed T, Larson JJ, et al. The role of three-dimensional magnetic resonance elastography in the diagnosis of nonalcoholic steatohepatitis in obese patients undergoing bariatric surgery. *Hepatology.* 2018. <https://doi.org/10.1002/hep.30483>.
- Pulli B, Wojtkiewicz G, Iwamoto Y, Ali M, Zeller MW, Bure L, et al. Molecular MR Imaging of myeloperoxidase distinguishes steatosis from steatohepatitis in nonalcoholic fatty liver disease. *Radiology.* 2017;284:390–400.
- Nativ NI, Chen AI, Yamush G, Henry SD, Lefkowitz JH, Klein KM, et al. Automated image analysis method for detecting and quantifying macrovesicular steatosis in hematoxylin and eosin-stained histology images of human livers. *Liver Transpl.* 2014;20:228–36.
- Schwen LO, Homeyer A, Schwieler M, Dahmen U, Dirsch O, Schenk A, et al. Zonated quantification of steatosis in an entire mouse liver. *Comput Biol Med.* 2016;73:108–18.
- Homeyer A, Hammad S, Schwen LO, Dahmen U, Hofener H, Gao Y, et al. Focused scores enable reliable discrimination of small differences in steatosis. *Diagn Pathol.* 2018;13:76.
- Deng M, Dahmen U, Sun J, Huang H, Sehestedt C, Homeyer A, et al. Limited correlation between conventional pathologist and automatic computer-assisted quantification of hepatic steatosis due to difference between event-based and surface-based analysis. *IEEE J Biomed Health Inform.* 2014;18:1473–7.
- Sethunath D, Morusu S, Tuceryan M, Cummings OW, Zhang H, Yin XM, et al. Automated assessment of steatosis in murine fatty liver. *PLoS ONE.* 2018;13:e0197242.
- Venturi C, Sempoux C, Quinones JA, Bourdeaux C, Hoyos SP, Sokal E, et al. Dynamics of allograft fibrosis in pediatric liver transplantation. *Am J Transpl.* 2014;14:1648–56.
- Jensen T, Abdelmalek MF, Sullivan S, Nadeau KJ, Green M, Roncal C, et al. Fructose and sugar: a major mediator of non-alcoholic fatty liver disease. *J Hepatol.* 2018;68:1063–75.
- Mahli A, Seitz T, Freese K, Frank J, Weiskirchen R, Abdel-Tawab M, et al. Therapeutic application of micellar solubilized xanthohumol in a western-type diet-induced mouse model of obesity, diabetes and non-alcoholic fatty liver disease. *Cells.* 2019;8:E359.
- Alwahsh SM, Xu M, Seyhan HA, Ahmad S, Mihm S, Ramadori G, et al. Diet high in fructose leads to an overexpression of lipocalin-2 in rat fatty liver. *World J Gastroenterol.* 2014;20:1807–21.
- Savard C, Tartaglione EV, Kuver R, Haigh WG, Farrell GC, Subramanian S, et al. Synergistic interaction of dietary cholesterol and dietary fat in inducing experimental steatohepatitis. *Hepatology.* 2013;57:81–92.
- Alwahsh SM, Gebhardt R. Dietary fructose as a risk factor for non-alcoholic fatty liver disease (NAFLD). *Arch Toxicol.* 2017;91:1545–63.
- Farrell G, Schattenberg JM, Leclercq I, Yeh MM, Goldin R, Teoh N, et al. Mouse models of nonalcoholic steatohepatitis: toward optimization of their relevance to human nonalcoholic steatohepatitis. *Hepatology.* 2019;69:2241–57.
- Farrell GC, Mridha AR, Yeh MM, Arsov T, Van Rooyen DM, Brooling J, et al. Strain dependence of diet-induced NASH and liver fibrosis in obese mice is linked to diabetes and inflammatory phenotype. *Liver Int.* 2014;34:1084–93.
- Larter CZ, Yeh MM, Haigh WG, Van Rooyen DM, Brooling J, Heydet D, et al. Dietary modification dampens liver inflammation and fibrosis in obesity-related fatty liver disease. *Obesity.* 2013;21:1189–99.

30. Legry V, Van Rooyen DM, Lambert B, Sempoux C, Poekes L, Espanol-Suner R, et al. Endoplasmic reticulum stress does not contribute to steatohepatitis in obese and insulin-resistant high-fat-diet-fed foz/foz mice. *Clin Sci*. 2014;127:507–18.
31. Ioannou GN, Van Rooyen DM, Savard C, Haigh WG, Yeh MM, Teoh NC, et al. Cholesterol-lowering drugs cause dissolution of cholesterol crystals and disperse Kupffer cell crown-like structures during resolution of NASH. *J Lipid Res*. 2015;56:277–85.
32. Haczeyni F, Poekes L, Wang H, Mridha AR, Barn V, Geoffrey HW, et al. Obeticholic acid improves adipose morphometry and inflammation and reduces steatosis in dietary but not metabolically obese mice. *Obesity*. 2017;25:155–65.
33. Mridha AR, Wree A, Robertson AAB, Yeh MM, Johnson CD, Van Rooyen DM, et al. NLRP3 inflammasome blockade reduces liver inflammation and fibrosis in experimental NASH in mice. *J Hepatol*. 2017;66:1037–46.
34. Liang JQ, Teoh N, Xu L, Pok S, Li X, Chu ESH, et al. Dietary cholesterol promotes steatohepatitis related hepatocellular carcinoma through dysregulated metabolism and calcium signaling. *Nat Commun*. 2018;9:4490.
35. Van Rooyen DM, Larter CZ, Haigh WG, Yeh MM, Ioannou G, Kuver R, et al. Hepatic free cholesterol accumulates in obese, diabetic mice and causes nonalcoholic steatohepatitis. *Gastroenterology*. 2011;141:1393–403. 1403
36. Haczeyni F, Wang H, Barn V, Mridha AR, Yeh MM, Haigh WG, et al. The selective peroxisome proliferator-activated receptor- δ agonist seladelpar reverses nonalcoholic steatohepatitis pathology by abrogating lipotoxicity in diabetic obese mice. *Hepatol Commun*. 2017;1:663–74.
37. Haczeyni F, Barn V, Mridha AR, Yeh MM, Estevez E, Febbraio MA, et al. Exercise improves adipose function and inflammation and ameliorates fatty liver disease in obese diabetic mice. *Obesity*. 2015;23:1845–55.
38. Poekes L, Gillard J, Farrell GC, Horsmans Y, Leclercq IA. Activation of brown adipose tissue enhances the efficacy of caloric restriction for treatment of nonalcoholic steatohepatitis. *Lab Investig*. 2019;99:4–16.
39. Wettstein G, Luccarini JM, Poekes L, Faye P, Kupkowski F, Adarbes V, et al. The new-generation pan-peroxisome proliferator-activated receptor agonist IVA337 protects the liver from metabolic disorders and fibrosis. *Hepatol Commun*. 2017;1:524–37.
40. Matsumoto M, Hada N, Sakamaki Y, Uno A, Shiga T, Tanaka C, et al. An improved mouse model that rapidly develops fibrosis in non-alcoholic steatohepatitis. *Int J Exp Pathol*. 2013;94:93–103.
41. Kodama Y, Kisseleva T, Iwaisako K, Miura K, Taura K, De MS, et al. c-Jun N-terminal kinase-1 from hematopoietic cells mediates progression from hepatic steatosis to steatohepatitis and fibrosis in mice. *Gastroenterology*. 2009;137:1467–77.
42. Wolf MJ, Adili A, Piotrowitz K, Abdullah Z, Boege Y, Stemmer K, et al. Metabolic activation of intrahepatic CD8⁺ T cells and NKT cells causes nonalcoholic steatohepatitis and liver cancer via cross-talk with hepatocytes. *Cancer Cell*. 2014;26:549–64.
43. Miura K, Kodama Y, Inokuchi S, Schnabl B, Aoyama T, Ohnishi H, et al. Toll-like receptor 9 promotes steatohepatitis by induction of interleukin-1 β in mice. *Gastroenterology*. 2010;139:323–34.
44. Itoh M, Kato H, Suganami T, Konuma K, Marumoto Y, Terai S, et al. Hepatic crown-like structure: a unique histological feature in non-alcoholic steatohepatitis in mice and humans. *PLoS ONE*. 2013;8:e82163.
45. Wyatt SK, Barck KH, Kates L, Zavala-Solorio J, Ross J, Kolumam G, et al. Fully-automated, high-throughput micro-computed tomography analysis of body composition enables therapeutic efficacy monitoring in preclinical models. *Int J Obesity*. 2015;39:1630–7.
46. Lubura M, Hesse D, Neumann N, Scherneck S, Wiedmer P, Schurmann A. Non-invasive quantification of white and brown adipose tissues and liver fat content by computed tomography in mice. *PLoS ONE*. 2012;7:e37026.
47. Fiorini RN, Kirtz J, Periyasamy B, Evans Z, Haines JK, Cheng G, et al. Development of an unbiased method for the estimation of liver steatosis. *Clin Transpl*. 2004;18:700–6.
48. Liquori GE, Calamita G, Cascella D, Mastrodonato M, Portincasa P, Ferri D. An innovative methodology for the automated morphometric and quantitative estimation of liver steatosis. *Histol Histopathol*. 2009;24:49–60.
49. El-Badry AM, Breitenstein S, Jochum W, Washington K, Paradis V, Rubbia-Brandt L, et al. Assessment of hepatic steatosis by expert pathologists: the end of a gold standard. *Ann Surg*. 2009;250:691–7.
50. Turlin B, Ramm GA, Purdie DM, Laine F, Perrin M, Deugnier Y, et al. Assessment of hepatic steatosis: comparison of quantitative and semiquantitative methods in 108 liver biopsies. *Liver Int*. 2009;29:530–5.
51. Roullier V, Cavarro-Menard C, Guillaume C, Aube C. Fuzzy algorithms to extract vacuoles of steatosis on liver histological color images. *Conf Proc IEEE Eng Med Biol Soc*. 2007;2007:5575–8.
52. Marsman H, Matsushita T, Dierkhising R, Kremers W, Rosen C, Burgart L, et al. Assessment of donor liver steatosis: pathologist or automated software? *Hum Pathol*. 2004;35:430–5.
53. d'Assignies G, Fontes G, Kauffmann C, Latour M, Gaboury L, Boulanger Y, et al. Early detection of liver steatosis by magnetic resonance imaging in rats infused with glucose and intralipid solutions and correlation to insulin levels. *Metabolism*. 2013;62:1850–7.
54. Zhang X, Fan L, Wu J, Xu H, Leung WY, Fu K, et al. Macrophage p38 α promotes nutritional steatohepatitis through M1 polarization. *J Hepatol*. 2019;71:163–74.
55. McGettigan B, McMahan R, Orlicky D, Burchill M, Danhorn T, Francis P, et al. Dietary lipids differentially shape nonalcoholic steatohepatitis progression and the transcriptome of Kupffer cells and infiltrating macrophages. *Hepatology*. 2018;70:67–83.
56. Roeb E. Matrix metalloproteinases and liver fibrosis (translational aspects). *Matrix Biol*. 2018;68-69:463–73.
57. Trautwein C, Friedman SL, Schuppan D, Pinzani M. Hepatic fibrosis: concept to treatment. *J Hepatol*. 2015;62:S15–S24.
58. Lackner C, Gogg-Kamerer M, Zatloukal K, Stumptner C, Brunt EM, Denk H. Ballooned hepatocytes in steatohepatitis: the value of keratin immunohistochemistry for diagnosis. *J Hepatol*. 2008;48:821–8.
59. Estep M, Mehta R, Brathauer G, Alparthi L, Monge F, Ali S, et al. Hepatic sonic hedgehog protein expression measured by computer assisted morphometry significantly correlates with features of non-alcoholic steatohepatitis. *BMC Gastroenterol*. 2019;19:27.
60. Guy CD, Suzuki A, Burchette JL, Brunt EM, Abdelmalek MF, Cardona D, et al. Costaining for keratins 8/18 plus ubiquitin improves detection of hepatocyte injury in nonalcoholic fatty liver disease. *Hum Pathol*. 2012;43:790–800.
61. Teufel A, Itzel T, Erhart W, Brosch M, Wang XY, Kim YO, et al. Comparison of gene expression patterns between mouse models of nonalcoholic fatty liver disease and liver tissues from patients. *Gastroenterology*. 2016;151:513–25.